https://doi.org/10.32604/zkg.2026.090849

ARTICLE

Development of sustainable engineered geopolymer composites incorporating yellow river silt and locally produced PVA fiber

Jiang Zhi[1], Jinxia Xu[1,*], Hanghui Wang[1] and Yingbin Song[2]
[1]College of Civil and Transportation, Hohai University, Nanjing, China
[2]Yellow River Institute of Hydraulic Research, Zhengzhou, China
*Corresponding Author: Jinxia Xu. Email: xujinxia@hhu.edu.cn

Received: 12 August 2026; Accepted: 21 September 2026

ABSTRACT: The incorporation of Yellow River Silt (YRS) and locally produced PVA (LP-PVA) fiber into engineered geopolymer composites (EGC) offers a promising strategy to mitigate the adverse environmental impacts and the cost of EGC. This paper evaluated the compressive and flexural strengths, uniaxial tensile performance and microstructure of fly ash-based EGC incorporating YRS and LP-PVA fiber. The influences of various factors, including water-to-precursor ratio (W/P), sand-to-precursor (S/P) ratio, and alkali content on the mechanical properties of as-fabricated EGC were carefully examined. The results indicate that as the W/P ratio increases and the S/P ratio decreases, the compressive strength, flexural strength, and tensile strength of as-fabricated EGC decrease, whereas the ultimate tensile strain increases. With raising alkali content, the compressive strength exhibits an initial rise followed by a reduction. In contrast, the flexural strength increases slightly, whereas the strain-hardening ability is compromised. Furthermore, a three-stage constitutive model for the as-fabricated EGC under uniaxial tensile loading has been successfully developed. The mechanical behavior should be attributed to the formation of denser N-A-S-H gel at higher alkali content.

KEYWORDS: Engineered geopolymer composites; YRS; LP-PVA fiber; mechanical properties; strain-hardening behavior

MATERIALS

1 Introduction

Engineered Cementitious Composites (ECC), a type of fiber-reinforced material, are distinguished by their exceptional ductility and multiple micro-cracking behavior, which effectively alleviate the intrinsic brittleness of conventional concrete [1]. These outstanding properties make ECC a promising material for an extensive range of engineering applications [2]. However, ECC is generally manufactured using fine aggregates alone, excluding the coarse aggregates typically incorporated in traditional concrete mixes [3]. As a result, ECC requires a significantly higher cement content, approximately two to three times that of ordinary concrete [3,4]. Cement production is widely recognized as one of the most environmentally damaging industrial processes owing to its significant energy demands combined with considerable CO_2 emissions [5–7]. Consequently, the elevated cement usage in ECC leads to considerably increased carbon footprints and energy demand [8,9]. Moreover, the extensive use of Silica sand and high-cost fiber (the most frequently used polyvinyl alcohol (PVA) and polyethylene (PE)) in ECC manufacturing further exacerbates ecological concerns and raises material costs [10,11]. These drawbacks collectively undermine the sustainability of ECC.

In response to the substantial environmental impact associated with the high cement content in ECC, researchers have been actively developing engineered geopolymer composites (EGC) [12]. A key feature of EGC is the complete replacement of cement with a geopolymer binder [13]. Unlike cement, geopolymer does not require high-temperature calcination and it is produced solely through the alkali activation of aluminosilicate precursors [14–16]. As a result, geopolymer is increasingly regarded as a viable and environmentally friendly alternative to cement [13]. While retaining high ductility and excellent crack control performance comparable to ECC, EGC reduces carbon dioxide emissions by approximately 80% and energy consumption by about 60% [17,18]. Owing to this combination of mechanical

performance and enhanced sustainability, EGC is suitable for a broader range of application scenarios than conventional ECC [19,20].

Despite the environmental advantages of EGC, several challenges remain for its practical engineering application. First, the workability of EGC is generally lower than that of ECC due to the viscous nature of alkali-activated systems, which hinders its large-scale application. Liu et al. [21] developed low-cost rubber crumb aggregate EGC and evaluated the influence of crumb rubber particle size and KH550 on its workability, mechanical properties, freeze–thaw resistance, and microstructure. The results showed that crumb rubber improved flowability, crack control, and freeze–thaw resistance, while KH550 enhanced the interfacial transition zone and fracture energy but reduced flowability and ultimate tensile strain. Second, the fire resistance of cementitious materials is critical for structural safety in tunnel and infrastructure applications. Zhang et al. [22] compared the spalling behaviors of alkali-activated ultra-high performance concrete (AAUHPC) and cement-based UHPC, revealing that AAUHPC exhibits superior spalling resistance due to its interconnected pore structure, which facilitates vapor pressure release during heating. Furthermore, the incorporation of supplementary cementitious materials has been shown to influence the high-temperature performance of cementitious matrices. Jiang et al. [23] investigated the effect of waste glass powder as a supplementary cementitious material on the physical and mechanical properties of cement paste under high temperatures, highlighting the potential of solid waste materials to improve fire resistance. These studies underscore the importance of addressing workability and durability challenges to advance the engineering application of sustainable cementitious composites.

To mitigate the environmental impact stemming from the widespread consumption of silica sand, a promising approach involves the utilization of various natural and recycled materials as alternatives. Liu et al. [21] investigated the freeze-thaw performance of low-cost rubber crumb aggregate EGC, demonstrating that crumb rubber particles not only improved crack control and freeze-thaw resistance but also imparted a particle-bridging mechanism that synergistically enhanced tensile ductility, with ultimate tensile strains reaching up to 9%. Yuan et al. [24] addressed the performance deterioration of EGC prepared with recycled fine aggregates (RFA) by introducing an in-situ generated nano-SiO_2 strategy through the condensation reaction between tannic acid and water glass, achieving a remarkable tensile strain capacity of 8.37% and a compressive strength of 99.2 MPa while significantly improving the matrix compactness. Woo et al. [25] developed calcium hydroxide-activated strain-hardening slag composites incorporating crumb rubber as a partial replacement for silica sand, demonstrating that the synergistic use of industrial by-products and recycled crumb rubber particles enabled a tensile strain capacity of 8.16% while substantially reducing CO_2 emissions and embodied energy. Zhang et al. [26] successfully developed EGC with an ultra-high tensile ductility of 8.4% using 100% coal gangue aggregates and up to 60% calcined coal gangue precursors under a low fiber dosage of 1.2%, highlighting the distinguished flaw effect of coal gangue aggregates in lowering cracking strength and enhancing tensile ductility. All these studies demonstrate that replacing quartz sand with solid waste-based fine aggregates not only facilitates the resource utilization of waste materials but also helps reduce the cost of EGC, supporting more sustainable construction practices.

The Yellow River, revered as China's "Mother River," carries the highest sediment load of any river in the world. With an annual sediment transport of 1.08 Gt/y, it accounts for approximately 6% of the global riverine sediment flux. Achieving the resource utilization of this vast amount of sediment is of critical importance for the protection of the Yellow River [27]. Our previous studies have shown that the YRS has an extremely fine mean particle size of approximately 185 µm, which renders it unsuitable for use as fine aggregate in ordinary concrete [28]. However, its size is remarkably close to that of Silica sand in traditional ECC and EGC. Moreover, the silt is chemically stable and mechanically robust, making it a potential alternative [28]. This assumption has been supported by the successful development of ECC using YRS [29]. However, whether the YRS can be applied to prepare the EGC or not remains unclear due to the loss of specific investigation.

The typical fiber dosage in EGC is 2% by volume. Currently, the reliance on expensive imported fibers, such as PVA fiber from Kuraray, constitutes a major cost driver. The high material cost subsequently impedes market acceptance of EGC. To address this issue, a practical solution is to substitute them with more cost-effective, LP-PVA fibers. Recent studies have demonstrated the feasibility of using domestic PVA fibers in engineered cementitious composites. Lu et al. [30] investigated the long-term tensile performance of ECC with high-volume fly ash and domestic PVA fibers, revealing that although the tensile strain capacity decreased with curing age due to the continuous increase in matrix fracture toughness and fiber/matrix interfacial bonding, the composites still exhibited distinct strain-hardening behavior with a tensile strain capacity exceeding 6% at 28 days. Qiu et al. [31] developed lower-cost ECC using locally produced PVA and PE fibers, and found that hybrid PVA-PE fiber reinforcement achieved an ultimate tensile strain exceeding 5.3% with an average crack width below 39 µm, demonstrating a positive hybrid reinforcing effect. Nevertheless, compared with the extensive investigations on ECC, research concerning the utilization of local PVA fibers in EGC remains scarce.

Based on these, this research is to develop a sustainable EGC incorporating YRS and LP-PVA fiber. The compressive and flexural strengths, uniaxial tensile performance and microstructure of fly ash-based EGC incorporating YRS and LP-PVA fiber are experimentally evaluated. The influences of various factors, including W/P ratio, S/P ratio, and alkali content on the mechanical properties of as-fabricated EGC were carefully examined. The microstructure of as-fabricated EGC was characterized by scanning electron microscopy (SEM), energy dispersive spectroscopy (EDS) and X-ray diffraction (XRD).

2 Experiment

2.1 Raw materials

Class F Grade I fly ash from Dengzhou Sitong Huajian Co., Ltd. was used. YRS was collected from the Liuzhuang section of Yellow River in Shandong Province. Table 1 shows the chemical compositions of fly ash and YRS. Figure 1 shows the images of YRS and fly ash. The physical properties of YRS are also provided. YRS has a specific gravity of 2.38 g/cm³, a bulk density of approximately 1420 kg/m³, and a water absorption of 1.53%. The mean particle size of YRS is approximately 185 µm with a fineness modulus of 1.8. Figure 2 shows the particle size distributions of YRS and fly ash. LP-PVA fibers from Anhui Wanwei Group Co., Ltd. were used. Its appearance is shown in Figure 3. Sodium silicate (water glass) from Jiashan Yourui Refractory Materials Co., Ltd. served as the main activator. NaOH (granular, analytical grade, purity ≥96.0%) from Guangdong Daxiao Chemical Co., Ltd. was used to adjust the modulus of the water glass. The experimental mix designs for EGC are displayed in Table 2.

2.2 Specimen preparation

EGC was prepared using a post-fiber mixing method with a planetary cement mixer [32]. First, NaOH granules were weighed and dissolved in the mixing water. The solution was stirred thoroughly

Table 1 Chemical components of fly ash and YRS

Chemical Composition	SiO_2	Al_2O_3	CaO	Fe_2O_3	K_2O	SO_3	MgO	Na_2O	LOI
Fly ash	43.00	28.00	9.60	11.8	1.65	0.80	0.95	1.10	3.10
YRS	60.11	13.42	10.33	6.30	4.01	0	1.58	1.61	/

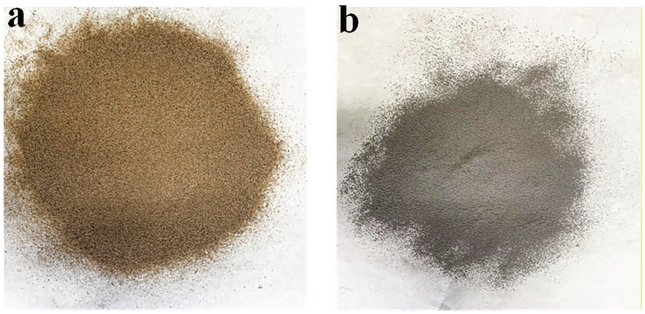


Figure 1 The images of YRS (a) and fly ash (b)

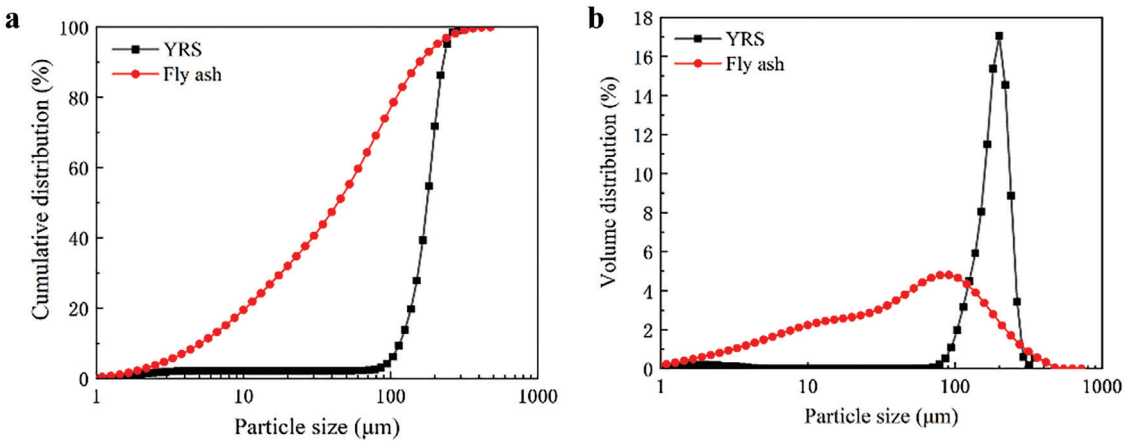


Figure 2 Particle size profiles of YRS and fly ash: (a) cumulative, (b) volume frequency



Figure 3 Appearance diagram of LP-PVA fibers

Table 2 The experimental mix designs for EGC

Mix ID	Fly Ash (g)	YRS (g)	Water Glass (g)	NaOH (g)	Extra Water (g)	PVA Fiber (g)
w0	1000	300	361.3	42	125.9	26
w1	1000	300	361.3	42	155.9	26
w2	1000	300	361.3	42	185.9	26
w3	1000	300	361.3	42	215.9	26
s1	1000	330	361.3	42	125.9	26
s2	1000	360	361.3	42	125.9	26
s3	1000	390	361.3	42	125.9	26
a1	1000	300	180.6	21	228	26
a2	1000	300	270.9	31.4	177	26
a3	1000	300	451.6	52.5	74.8	26

and cooled to room temperature. The cooled NaOH solution was added to the pre-weighed water glass solution, mixed uniformly, and brought to ambient temperature, adjusting the modulus of the original water glass from 2.3 to 1.4. Second, fly ash and sand were weighed, added to the mixing bowl, and dry-mixed at low speed for 1 min. Third, the modulus-adjusted water glass solution was added to the mixing bowl and mixed at high speed for 4 min. Fourth, fibers were added uniformly during low-speed mixing. After all fibers were added, mixing proceeded vigorously for 4 min. Finally, the mixed EGC mortar was cast into molds, vibrated for 1–2 min, leveled with a steel ruler, and covered with a polyethylene film. Specimens were placed in an oven at 60°C for 12–24 h before demolding. After demolding, specimens were transferred to a standard curing chamber for 28 days.

In accordance with Chinese standard GB/T 17671-2021 [33], prismatic specimens with the size of 4 × 4 × 16 cm^3 were used to measure compressive and flexural strength. Dogbone shaped specimen of as-fabricated EGC was utilized to the tensile test, as shown in Figure 4.

2.3 Testing methods

2.3.1 Compressive and flexural strength

A servo-controlled universal testing machine applied a vertical load uniformly to the sides of the prism at a rate of 50 N/s ± 10 N/s until fracture. Three prismatic specimens per group were tested.

After flexural strength tests, the resulting six fragments were used for compressive strength testing. Smaller fragments were positioned in specialized molds to ensure a 40 mm × 40 mm loading surface. The mold containing the specimen was placed under a micro-electro-hydraulic servo pressure testing machine and loaded uniformly at a rate of 2400 N/s ± 200 N/s until failure.

2.3.2 Uniaxial tensile test

A DNS100 electronic universal testing machine was employed and loading was applied under displacement control at 0.5 mm/min until failure. Strain in the central portion of the tensile specimen was measured using an extensometer and a dynamic stress-strain gauge. After tensile fracture, small samples were sectioned from the fracture surface for SEM analysis. The specimen dimensions and test setup for the uniaxial tensile test are shown in Figure 4.

2.3.3 Microstructural analysis

The microstructure of fracture surfaces of EGC specimens after tensile testing was observed using SEM, EDS and XRD were employed to qualitatively analyze the phase composition of the EGC matrix and identify hydration products, providing

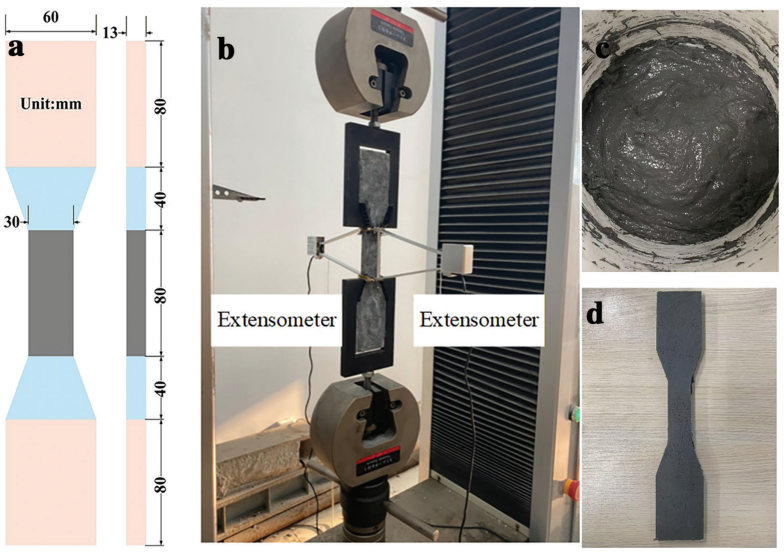


Figure 4 Specimen (a), experimental test device (b) for uniaxial tensile test, (c) freshly mixed EGC mortar before casting, and (d) dogbone-shaped tensile specimen

experimental evidence to elucidate the relationship between the material's mechanical properties and its microstructure. For SEM imaging, an accelerating voltage of 3 kV was used. For EDS analysis, the accelerating voltage was set to 20 kV. XRD measurements were conducted at 40 kV, with a scanning range of 10° to 80° and a scanning speed of 2°/min.

3 Results and discussion

3.1 Mechanical properties of as-fabricated EGC

3.1.1 Influence of W/P ratio

Figure 5 illustrates the variation trends of compressive and flexural strengths of fly ash-based EGC incorporating YRS under various W/P ratio conditions. As the W/P ratio rises from 0.33 to 0.42, the compressive strength of EGC reduces from 19.7 MPa to 12.8 MPa, a decrease of 35.0%, exhibiting a nearly linear declining trend. The flexural strength reduces from 7.2 MPa to 4.6 MPa, a decrease of 36.1%. The decline trend of flexural strength is essentially consistent with that of compressive strength, albeit with slightly higher sensitivity. The primary reason is that the difference in sensitivity of compressive and flexural strength to the W/P ratio may be related to the failure mode. Flexural strength is more significantly influenced by material surface defects and interfacial bonding performance, whereas compressive strength relies more on the overall compactness of the matrix [34]. A higher W/P ratio causes a higher free water content. After water evaporation during curing, more pores are formed, reducing material compactness and consequently weakening the strength. Excessive water might dilute the concentration of the

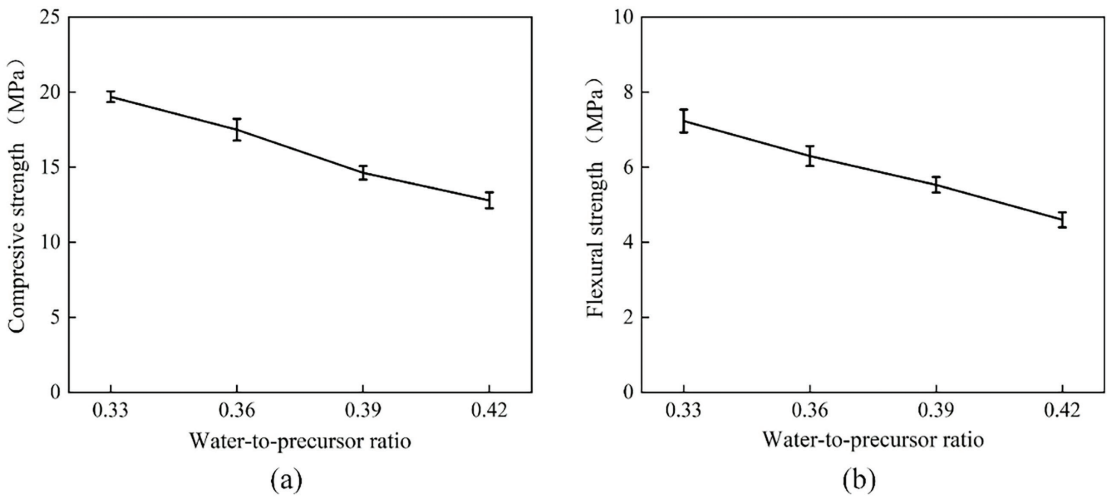


Figure 5 Compressive strength (a) and flexural strength (b) of EGC with different W/P ratios. (w0: 0.33, w1: 0.36, w2: 0.39, w3: 0.42)

alkaline activator, thereby inhibiting the dissolution and polycondensation reactions of aluminosilicates in the fly ash, resulting in a greater proportion of incompletely reacted gel structures, affecting the overall strength. The bond strength between fibers and the matrix in EGC is sensitive to the W/P ratio. A high W/P ratio may weaken the interfacial transition zone, exacerbating crack propagation [35]. The research results demonstrate that the W/P ratio is a predominant factor for regulating the mechanical properties of EGC, and its increase significantly reduces both compressive and flexural strength.

Figure 6 shows the tensile cracking characteristics of EGC with different W/P ratios after tensile testing. Similar to the tensile cracking characteristics of ECC, as the W/P ratio rises from 0.33 to 0.42, the number of cracks on the specimen surface during tensile failure gradually increases, and the crack spacing gradually decreases. It is observable that a higher W/P ratio facilitates further crack propagation.

The uniaxial tensile stress-strain curves of EGC under various W/P ratios are shown in Figure 7. Table 3 summarizes the first-crack strength (f_0), tensile strength (f_u), and ultimate tensile strain (ε_t). As the W/P ratio rises from 0.33 to 0.42, both the first-crack strength and tensile strength of EGC decrease significantly. The first-crack strength declines from 1.99 MPa to 1.34 MPa, a decrease of 32.7%. The tensile strength declines from 2.57 MPa to 1.99 MPa, a decrease of 22.6%. The decrease in strength is mainly ascribed to the increased dispersion of cementitious materials and increased porosity under high W/P ratio conditions. The rise of W/P ratio causes a reduction in the content of effective cementitious material per unit volume, and the microstructure tends to become looser, thus weakening the matrix's bonding capacity to the fibers and reducing the load-bearing efficiency of the overall structure. Under the 0.42 W/P ratio condition, the error range of the tensile strength (±0.11 MPa) is significantly larger than other groups, indicating

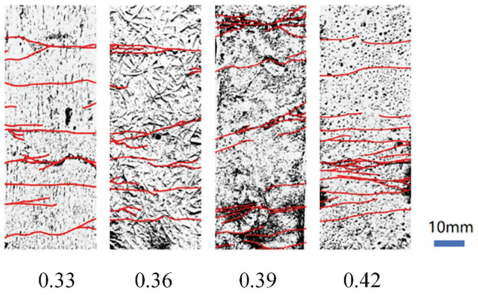


Figure 6 Crack patterns of EGC with different W/P ratios

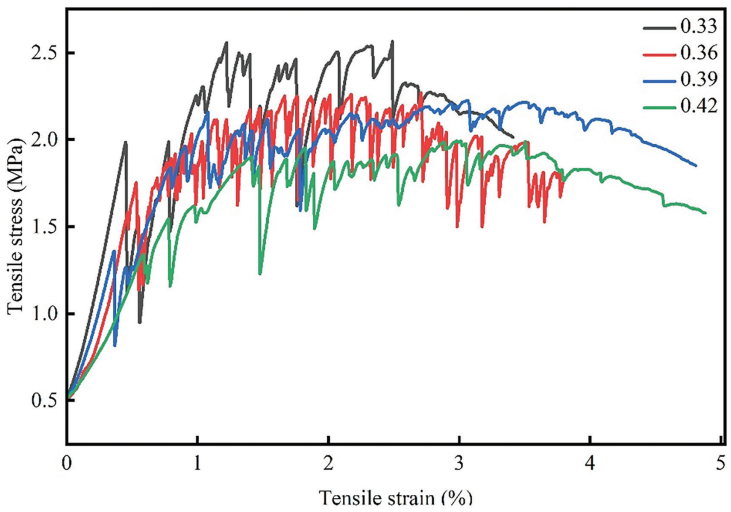


Figure 7 Tensile behaviour of EGC with different W/P ratios

Table 3 Tensile performance parameters of EGC with different W/P ratios

W/P	f_0 (MPa)	f_u (MPa)	ε_t (%)
0.33	1.99 ± 0.06	2.57 ± 0.07	3.41 ± 0.08
0.36	1.75 ± 0.08	2.27 ± 0.05	3.53 ± 0.11
0.39	1.36 ± 0.03	2.23 ± 0.06	4.38 ± 0.06
0.42	1.34 ± 0.04	1.99 ± 0.11	4.57 ± 0.12

poorer uniformity of EGC material performance at this W/P ratio, possibly affected by uneven water distribution or differential shrinkage during the hardening process. The ultimate tensile strain of EGC rises with the increase of the W/P ratio, rising from 3.41% to 4.57%, an increase of 34.1%. Under high W/P ratio conditions, EGC undergoes a longer stage of plastic deformation before fracture, indicating that the increase of the W/P ratio enhances the strain-hardening capacity of EGC. However, this improvement in ductility comes at the cost of sacrificing some tensile strength. In practical engineering applications, a trade-off between strength and ductility is required based on specific needs.

3.1.2 Influence of S/P ratio

Figure 8 shows the variation trends of compressive and flexural strengths of EGC under different S/P ratio conditions. The experimental results indicate that when the S/P ratio rises from 0.30 to 0.39, both the compressive and flexural strengths of EGC show significant positive correlation growth. The compressive strength rises from 19.7 MPa to 22.3 MPa, a rise of 12.7%. The flexural strength rises from 7.2 MPa to 8.7 MPa, a rise of 20.8%. This may be because sand particles fill the pores of the cementitious material, reducing defects and enhancing overall compactness and compressive strength. Additionally, the interfacial bonding between sand and the cementitious material is enhanced, improving stress transfer efficiency, and the increase in sand content may inhibit crack propagation by forming a denser fiber-matrix interface, thereby improving flexural performance. Within the S/P ratio range of 0.30~0.39, both the compressive and flexural strengths of EGC rise substantially with the rise of the S/P ratio. It should be noted that the S/P ratio range in this test did not cover the critical value. When the S/P ratio is too high, insufficient cementitious material may lead to decreased interfacial adhesion [36,37].

Figure 9 displays the tensile cracking patterns of EGC with different S/P ratios. It can be intuitively observed that as the S/P ratio rises from 0.30 to 0.39, the number of cracks in EGC gradually decreases, especially the number of coherent long cracks. The specimen transitions from relatively uniform long crack failure to short crack failure with stress concentration.

The uniaxial tensile stress-strain curves of EGC under various S/P ratios are shown in Figure 10. Table 4 concludes f_0, f_u, and ε_t. When the S/P ratio rises from 0.30 to 0.39, the first-crack strength

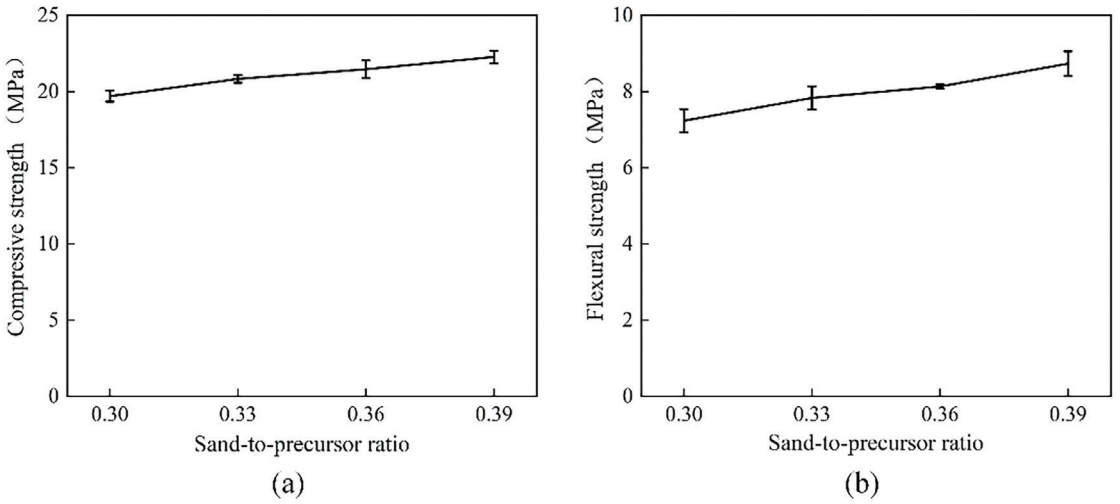


Figure 8 Compressive strength (a) and flexural strength (b) of EGC with different S/P ratios. (w0: 0.30, s1: 0.33, s2: 0.36, s3: 0.39).

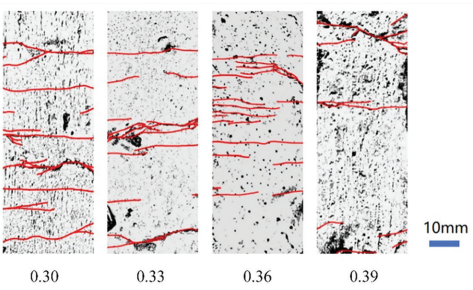


Figure 9 Crack patterns of EGC with different S/P ratios

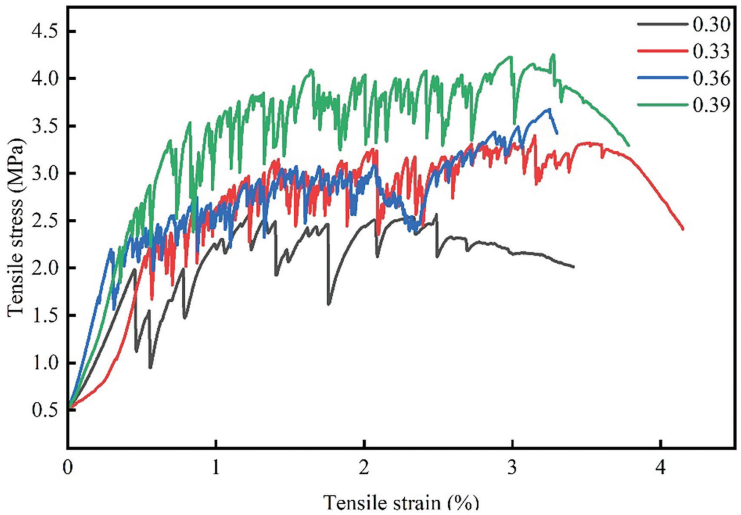


Figure 10 Tensile behaviour of EGC with different S/P ratios

Table 4 Tensile performance parameters of EGC with different S/P ratios

S/P	f_0 (MPa)	f_u (MPa)	ε_t (%)
0.30	1.99 ± 0.06	2.57 ± 0.07	3.41 ± 0.08
0.33	2.12 ± 0.05	3.40 ± 0.04	3.37 ± 0.05
0.36	2.20 ± 0.05	3.60 ± 0.03	3.30 ± 0.07
0.39	2.22 ± 0.04	4.25 ± 0.05	3.28 ± 0.10

rises from 1.99 MPa to 2.22 MPa, an increase of 11.6%. This demonstrates that the addition of sand particles effectively improves the material's ability to resist initial cracking. This may be because sand particles fill the pores in the cementitious matrix, optimizing the compactness of the microstructure, thereby enhancing the load-bearing capacity of the matrix in the early stage of tension. Furthermore, the interfacial bonding strength between sand and the matrix may improve with increasing sand content, further inhibiting the development of early cracks. The tensile strength also rises with the rise of the S/P ratio, rising from 2.57 MPa at a S/P ratio of 0.30 to 4.25 MPa at a S/P ratio of 0.39, an increase of 65.4%. This trend is consistent with the growth trend of the first-crack strength, indicating that the rise of S/P ratio not only boosts the crack resistance of the material but also enhances its tensile performance. The incorporation of sand particles may improve the stress transfer efficiency of the matrix by dispersing stress, delaying crack propagation paths, and through frictional influences, thereby increasing the ultimate tensile strength of the material. Additionally, the ultimate tensile strain shows a decreasing trend with the rise of the S/P ratio, decreasing from 3.41% at a S/P ratio of 0.30 to 3.28% at a S/P ratio of 0.39, a reduction of 3.8%. This demonstrates that the rise of S/P ratio enhances the stiffness of the material but sacrifices its ductility. Excessive sand particles may increase the brittleness of the matrix, weakening the material's plastic deformation capacity before fracture.

3.1.3 Influence of alkali content

Figure 11 shows the variation trends of compressive and flexural strengths of EGC under different alkali content conditions. The experimental results show that when the alkali content is 4%, 6%, 8%, and 10%, the compressive strengths are 16.0 MPa, 18.0 MPa, 19.7 MPa, and 18.4 MPa, respectively, with the peak appearing at 8% content. For the corresponding alkali content, the flexural strengths are 4.7 MPa, 6.2 MPa, 7.2 MPa, and 7.9 MPa, respectively, showing a monotonically increasing trend, but the growth rate gradually decreases (increases of 31.9%, 16.1%, and 9.7%, respectively). Possible reasons include: The increase in alkali content promotes the alkali activation reaction, generating dense N-A-S-H gel, which enhances matrix compactness [38,39]. However, excessive alkali content leads to non-uniform gel distribution and the formation of weak zones, explaining the decrease in compressive strength beyond 8% [40]. Flexural strength is more dependent on fiber-matrix interfacial bonding than on matrix compactness. Higher alkali content strengthens the chemical and frictional bond between PVA fibers and the geopolymer matrix, leading to a continuous increase in flexural strength.

Figure 12 displays the tensile cracking patterns of EGC with different alkali contents. When the

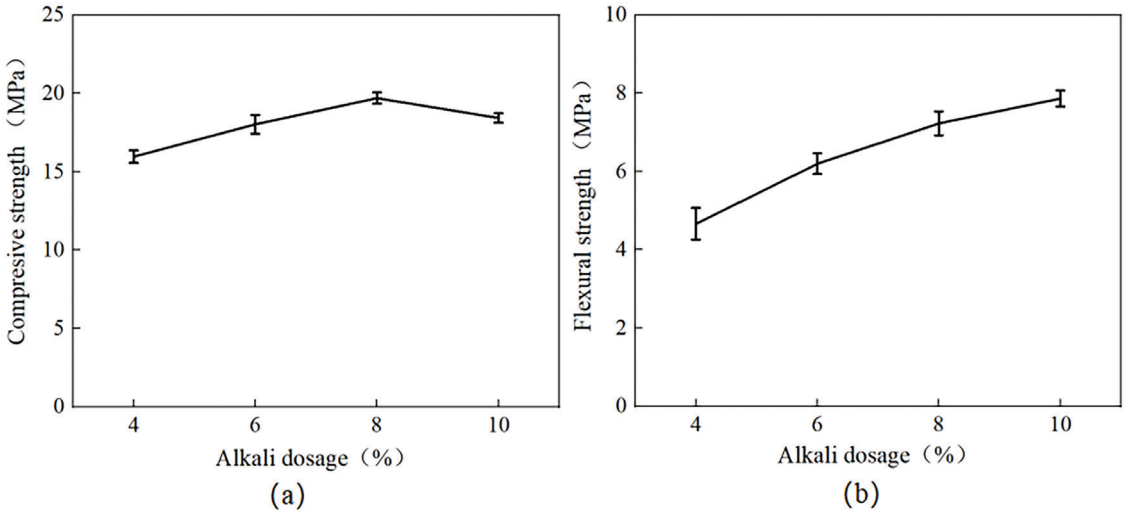


Figure 11 Compressive strength (a) and flexural strength (b) of EGC with various alkali dosages. (a1: 4%, a2: 6%, w0: 8%, a3: 10%)

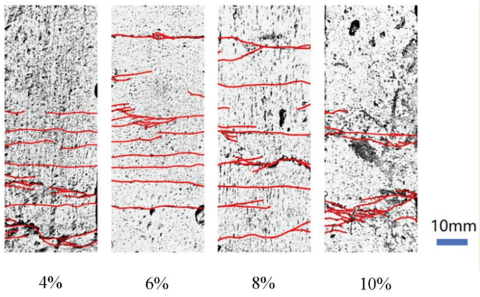


Figure 12 Crack patterns of EGC with various alkali dosages

alkali content is below 10%, the specimen cracks are evenly distributed, whereas at 10% alkali content, the cracks show a concentrated distribution. This may be owing to the uneven reaction of particles under high alkali concentration, forming weak interfaces between the generated gel and unreacted areas, prompting cracks to preferentially propagate along these paths.

The uniaxial tensile stress-strain curves of EGC under different alkali contents are shown in Figure 13. Table 5 concludes f_0, f_u, and ε_t. When the alkali content rises from 4% to 10%, the first-crack strength of EGC declines from 2.48 MPa to 1.92 MPa, a decrease of 22.6%. The tensile strength declines from 3.67 MPa to 2.42 MPa, a decrease of 34.11%, and the ultimate tensile strain

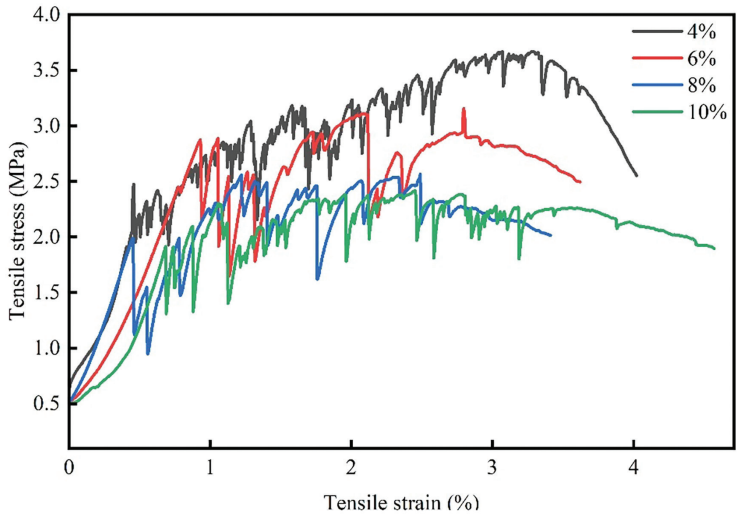


Figure 13 Tensile behaviour of EGC with various alkali dosages

Table 5 Tensile performance parameters of EGC with various alkali dosages

Alkali Dosages	f_0 (MPa)	f_u (MPa)	ε_t (%)
4%	2.48 ± 0.07	3.67 ± 0.10	3.61 ± 0.08
6%	2.45 ± 0.05	3.16 ± 0.11	3.47 ± 0.09
8%	1.99 ± 0.06	2.57 ± 0.07	3.41 ± 0.08
10%	1.92 ± 0.05	2.42 ± 0.04	3.30 ± 0.07

reduces from 3.61% to 3.30%, a decrease of 8.6%. It can be noted that as the alkali content rises, the mechanical properties of EGC continuously weaken. When the alkali content exceeds 8%, the decline amplitude of each parameter intensifies to a greater extent, indicating that high alkali content has a more significant negative effect on material performance. Combined with the stress-strain curve graph, it can be intuitively found that as the alkali content increases, the strain-hardening behavior of EGC gradually weakens. Possible reasons include: Tensile properties are primarily governed by the strain-hardening behavior, which requires a balanced combination of matrix toughness and fiber bridging. At high alkali content, the matrix becomes overly brittle, and the interfacial bonding becomes too strong, making it difficult for fibers to gradually debond and bridge cracks. This leads to reduced crack-bridging efficiency and fewer multiple cracks, resulting in a consistent decrease in tensile properties. Additionally, strong alkaline conditions at elevated temperatures can degrade PVA fibers, further reducing fiber strength and toughness.

3.2 Constitutive model for as-fabricated EGC under uniaxial tensile loading

The simplified model for the widespread uniaxial tensile stress-strain curve of EGC is illustrated in Figure 14, and its calculation formula is given by Eq. (1). The model can be primarily categorized into the following three stages.

1. Linear elastic stage: In this stage, no visible cracks develop, and the original stress-strain curve is nearly linear. The stage ends at σ_p, which represents the first-crack stress, and ε_p, which denotes the first-crack strain.
2. Strain-hardening stage: During this phase, cracks begin to propagate, and their number increases relatively uniformly with increasing strain. The stage concludes at σ_b, indicating the peak stress, and ε_b, representing the peak strain.
3. Strain-softening stage: In this stage, the stress-strain curve begins to decline. Fibers undergo stretching and damage, while the number and width of cracks continue to rise, and the load-bearing capacity decreases with fluctuation. When one crack develops into a dominant crack, the specimen fails at that location. At this point, σ_u denotes the ultimate tensile stress, and ε_u represents the ultimate tensile strain. The coefficients α and β are introduced as correction factors to account for the influence of different parameters.

$$\sigma = \begin{cases} \dfrac{\sigma_p}{\varepsilon_p}\varepsilon\, 0 \le \varepsilon < \varepsilon_p \\ \sigma_p + \alpha\dfrac{\sigma_b - \sigma_p}{\varepsilon_b - \varepsilon_p}\left(\varepsilon - \varepsilon_p\right)\varepsilon_p \le \varepsilon \le \varepsilon_b \\ \sigma_b + \beta\dfrac{\sigma_u - \sigma_b}{\varepsilon_u - \varepsilon_b}\left(\varepsilon - \varepsilon_b\right)\varepsilon_b \le \varepsilon \le \varepsilon_u \end{cases} . \quad (1)$$

EGC groups with a relatively obvious strain hardening stage under different influencing factors were selected for fitting analysis. The EGC tensile stress-strain curves and fitting curves are displayed in Figure 15. The tensile mechanical parameters and the obtained correction coefficients α and β are shown in Table 6. By analyzing the data in the table, the changes in the correction coefficients under different influencing factors are examined. It can be observed that changes in the W/P ratio have a significant influence on the fluctuation of the correction coefficient α for the strain hardening stage of EGC, while the impact on the fluctuation of the correction coefficient β for the strain softening stage is relatively small. This indicates that the W/P ratio mainly affects the stable progression of the strain hardening stage of EGC, a characteristic consistent with ECC. Changes in the S/P ratio have a greater impact on the fluctuation of α and a slightly smaller impact on β, meaning the S/P ratio mainly affects the stability of the strain hardening stage of EGC. The alkali content has a greater impact on the fluctuation of both α and β, demonstrating that the alkali content has a considerable influence on the stability of both the strain hardening and strain softening stages of EGC. Possible reasons include: α reflects the stability of multiple cracking, which is governed by matrix toughness and uniformity. The W/P and S/P ratios mainly affect matrix compactness and pore structure, thus directly influencing α. β reflects post-peak fiber bridging and pullout behavior, which is controlled by fiber-matrix interfacial bonding. The W/P and S/P ratios do not significantly alter interfacial chemistry, so their influence on β is small. Alkali content affects both stages because it alters the gel chemistry and microstructure, which influences matrix toughness (α) and fiber-matrix interfacial bonding (β). Higher alkali content also affects PVA fiber durability, further impacting bridging capacity.

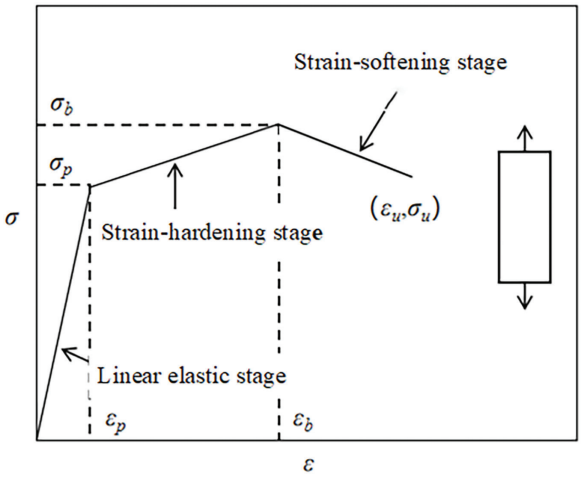


Figure 14 **Simplified model of uniaxial tensile stress-strain for EGC**

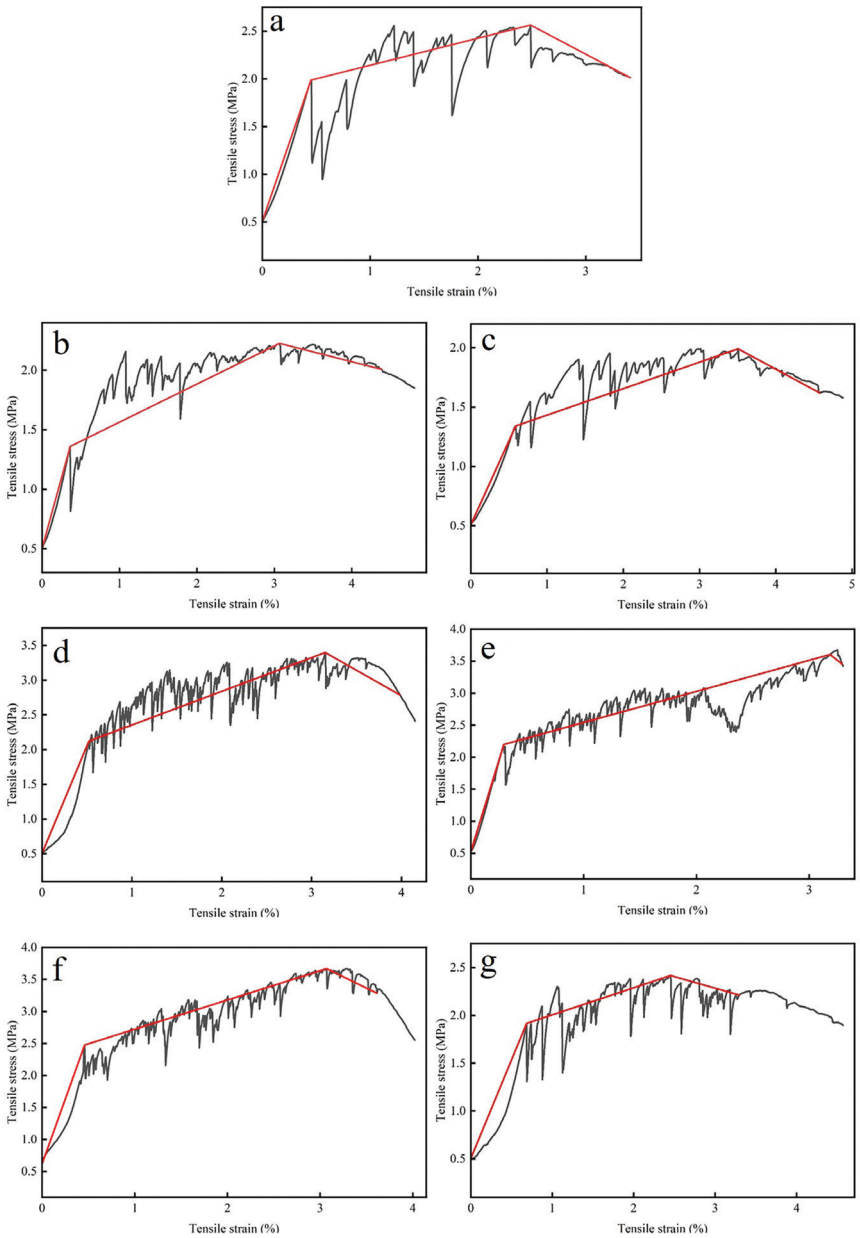


Figure 15 **The tensile stress-strain curve and fitting curve of EGC: w0 (a), w2 (b), w3 (c), s1 (d), s2 (e), a1 (f), a3 (g)**

Table 6 Tensile mechanical parameters and fitting correction coefficients of EGC

Number	σ_p/MPa	ε_p/%	σ_b/MPa	ε_b/%	σ_u/MPa	ε_u/%	α	β
w0	1.99	0.45	2.57	2.49	2.02	3.41	1.67 ± 0.03	1.58 ± 0.12
w2	1.36	0.36	2.23	3.07	2.01	4.38	1.24 ± 0.02	1.72 ± 0.11
w3	1.34	0.59	1.99	3.50	1.62	4.57	0.69 ± 0.01	1.49 ± 0.13
s1	2.12	0.52	3.40	3.15	3.20	3.37	1.57 ± 0.03	1.44 ± 0.10
s2	2.20	0.29	3.60	3.18	3.45	3.30	1.41 ± 0.02	1.61 ± 0.14
a1	2.48	0.46	3.67	3.07	3.29	3.61	1.38 ± 0.01	1.62 ± 0.12
a3	1.92	0.68	2.42	2.45	2.12	3.30	1.02 ± 0.02	1.13 ± 0.07

3.3 Microstructural observation

SEM images of EGC are shown in Figure 16. Compare the surface conditions of the a1 specimen and a3 specimen. It can be clearly found that there are numerous indentations left after fiber pull-out on the surface of the a1 specimen. These indentations are relatively dense, intuitively reflecting the bonding condition between the fibers and the matrix. In contrast, such indentations are relatively fewer on the surface of the a3 specimen. It is inferred that under higher alkali content, the interfacial bonding force between the EGC matrix and the fibers is stronger, and the fibers experience greater friction during the pull-out process. SEM images and EDS image of EGC are shown in Figure 17. Comparing Figures a and b, it can be seen that the a1 specimen appears relatively loose, with many unreacted smooth spherical fly ash particles showing no obvious etching marks, while the a3 specimen is tight, structurally dense, and accompanied by microcracks. This also verifies that high alkali content improves the compactness and strength of the matrix, and the expansion of microcracks also helps to improve the flexural strength and strain hardening behavior of a3 specimen. This is mainly because the low concentration of OH^- in a low alkali environment inhibits the dissolution process of fly ash particles and the rate of the silicate-aluminate polycondensation reaction [41]. In the clustered and flocculent particles in Figures c and d, the particle size is about 100 nm. Its EDS spectrum is shown in Figure e, which is mainly composed of Si, Al, Na, and O elements. It is judged that these particles are N-A-S-H gel [42]. However, given the presence of CaO in both fly ash and YRS, the coexistence of C-A-S-H or C-(N)-A-S-H gels cannot be excluded. Calcium may participate in the geopolymerization reaction, forming a hybrid gel structure. High alkali content promotes the activation reaction, generating dense gel particles, which corresponds to the rise of compressive strength with higher alkali content.

The phase composition of YRS, fly ash, a3 specimen, and a1 specimen was tested using XRD technology. The XRD patterns are shown in Figure 18. Observing the XRD pattern of the raw material YRS, the characteristic peaks of quartz and calcite can be clearly seen. Then, in the XRD pattern of EGC, the characteristic peaks of quartz have disappeared, indicating that it has been dissolved, participated in the relevant reaction, and the reaction is relatively complete. The XRD patterns of the two EGCs are roughly similar, indicating that EGC has a similar mineral composition within this alkali content range. The calcite characteristic peak in EGC may come from that carried by the YRS, and mullite comes from fly ash, which basically does not participate in the reaction at alkali contents of 4%~10%. In fly ash geopolymer EGC, the XRD pattern of N-A-S-H gel is mainly a broadened amorphous "hump peak" [43]. Compared to the XRD pattern of a1 specimen, the broad peak of N-A-S-H gel in a3 specimen is more obvious, the peak shape is sharper, and it shifts towards higher angles, indicating that more gel phase is produced and the structure is more ordered. It can be deduced that increasing the alkali concentration can promote the reaction and reduce unreacted crystalline phases.

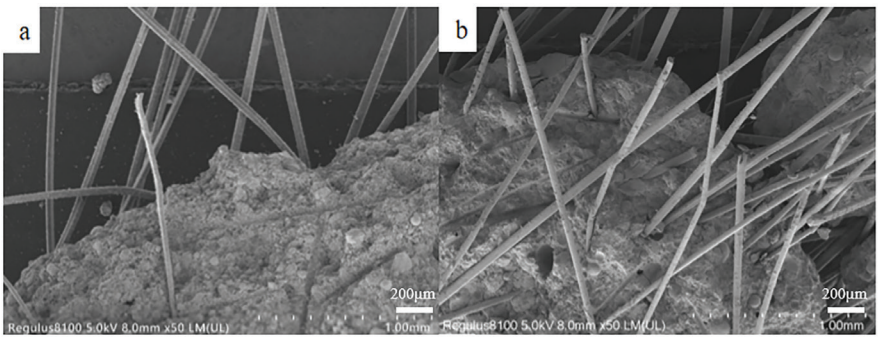


Figure 16 SEM images of EGC: a1 specimen (a), a3 specimen (b)

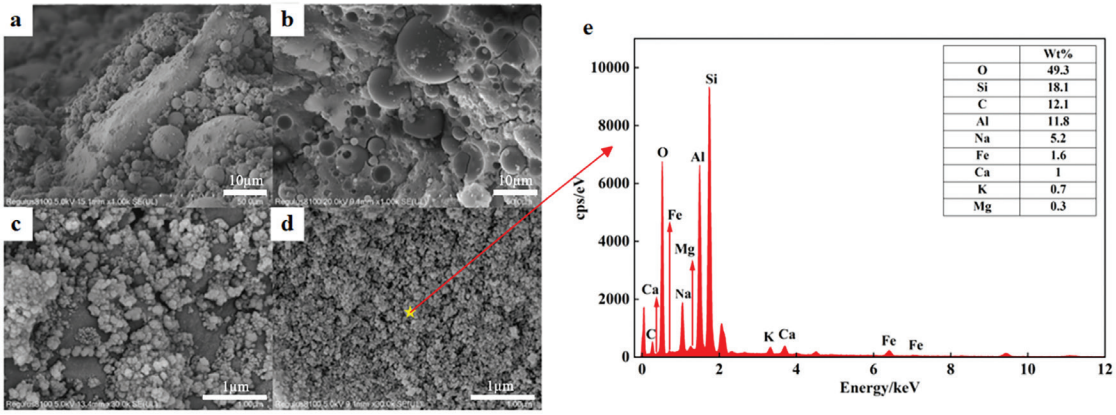


Figure 17 SEM images of EGC specimens a1 (a, c) and a3 (b, d), with EDS spectrum (e) from the asterisk in (d)

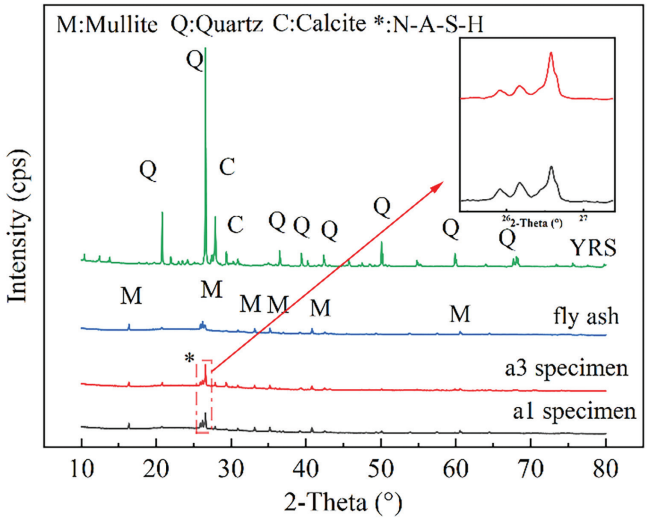


Figure 18 XRD patterns of YRS, fly ash, a3 specimen, a1 specimen

4 Conclusion

This study develops a sustainable engineered geopolymer composite (EGC) incorporating Yellow River silt (YRS) and locally produced PVA (LP-PVA) fiber. The compressive and flexural strengths, uniaxial tensile performance, and microstructure of fly ash-based EGC containing YRS and LP-PVA fiber are experimentally evaluated. The influences of various factors, including the water-to-precursor (W/P) ratio, sand-to-precursor (S/P) ratio, and alkali content, on the mechanical properties of the as-fabricated EGC are systematically investigated. The main conclusions are as follows.

(1) The compressive strength, flexural strength, and tensile strength of EGC all decrease as the W/P ratio increases, exhibiting an approximately linear negative correlation. However, an increase in the W/P ratio improves the ultimate tensile strain and enhances the ductility of EGC. The W/P ratio is a key parameter for regulating the mechanical properties of EGC; therefore, a balance between strength and ductility needs to be optimized for engineering applications.

(2) When the S/P ratio ranges from 0.30 to 0.39, the compressive strength, flexural strength, first-crack strength, and tensile strength all increase with increasing S/P ratio, whereas the ultimate tensile strain decreases from 3.41% to 3.28%. Within this range, increasing the S/P ratio enhances the strength of EGC but reduces its ductility.

(3) As the alkali content increases from 4% to 10%, the compressive strength first increases and then decreases, reaching a maximum at an alkali content of 8%. In contrast, the flexural strength continues to increase with increasing alkali content, although the rate of increase gradually decreases. The uniaxial tensile performance decreases significantly with increasing alkali content, and the strain-hardening behavior of EGC is weakened.

(4) A three-stage constitutive model, comprising a linear elastic stage, a strain-hardening stage, and a strain-softening stage, is developed for the as-fabricated EGC under

uniaxial tensile loading. The W/P and S/P ratios have a major influence on the correction coefficient α for the strain-hardening stage but only a minor influence on the correction coefficient β for the strain-softening stage. In addition, the alkali content significantly affects both α and β.

(5) The main reaction product of EGC is flocculent or clustered N-A-S-H gel particles. Increasing the alkali content promotes the activation reaction, generates more N-A-S-H gel particles, and improves the compactness and strength of the matrix.

Acknowledgement

Authors gratefully acknowledge the financial support from Natural Science Foundation of China (No. 52371276).

Funding Statement

This research is funded by the National Natural Science Foundation of China (Grant No. 52371276).

Author Contributions

Jiang Zhi: investigation, formal analysis, data curation, writing—original draft. Jinxia Xu: conceptualization, methodology, supervision, writing—review & editing, funding acquisition. Hanghui Wang: investigation, data curation, visualization. Yingbin Song: resources, validation, writing—review & editing. All authors reviewed and approved the final version of the manuscript.

Availability of Data and Materials

The data supporting the findings of this study are available from the corresponding author upon reasonable request.

Ethics Approval

Not applicable.

Conflicts of Interest

The authors declare no conflicts of interest.

REFERENCES

[1] Li VC, Leung CKY. Steady-state and multiple cracking of short random fiber composites. J Eng Mech. 1992;118(11):2246–64. doi:10.1061/(asce)0733-9399(1992)118:11(2246).
[2] Mechtcherine V. Novel cement-based composites for the strengthening and repair of concrete structures. Constr Build Mater. 2013;41(2):365–73. doi:10.1016/j.conbuildmat.2012.11.117.
[3] Yang EH, Yang YZ, Li VC. Use of high volumes of fly ash to improve ECC mechanical properties and material greenness. ACI Mater J. 2007;104(6):620. doi:10.14359/18966.
[4] Gartner E. Industrially interesting approaches to "low-CO_2" cements. Cem Concr Res. 2004;34(9):1489–98. doi:10.1016/j.cemconres.2004.01.021.
[5] Teixeira ER, Mateus R, Camões A, Branco FG. Quality and durability properties and life-cycle assessment of high volume biomass fly ash mortar. Constr Build Mater. 2019;197:195–207. doi:10.1016/j.conbuildmat.2018.11.173.
[6] Wei J, Cen K. Empirical assessing cement CO_2 emissions based on China's economic and social development during 2001–2030. Sci Total Environ. 2019;653:200–11. doi:10.1016/j.scitotenv.2018.10.371.
[7] Bărbulescu A, Hosen K. Cement industry pollution and its impact on the environment and population health: a review. Toxics. 2025;13(7):587. doi:10.3390/toxics13070587.
[8] Lei D, Jia H, Yu L, Li Y, Wu Z, Wang B, et al. Recent developments in low-carbon engineered cementitious composites (ECC). J Build Eng. 2025;100(4):111734. doi:10.1016/j.jobe.2024.111734.
[9] Elmesalami N, Celik K. A critical review of engineered geopolymer composite: a low-carbon ultra-high-performance concrete. Constr Build Mater. 2022;346:128491. doi:10.1016/j.conbuildmat.2022.128491.
[10] Xu LY, Huang BT, Dai JG. Development of engineered cementitious composites (ECC) using artificial fine aggregates. Constr Build Mater. 2021;305(2):124742. doi:10.1016/j.conbuildmat.2021.124742.
[11] Yu JH, Li VC. Research on production, performance and fibre dispersion of PVA engineering cementitious composites. Mater Sci Technol. 2009;25(5):651–6. doi:10.1179/174328408X327731.
[12] Kan LL, Lv JW, Duan BB, Wu M. Self-healing of engineered geopolymer composites prepared by fly ash and metakaolin. Cem Concr Res. 2019;125:105895. doi:10.1016/j.cemconres.2019.105895.
[13] Alhawat M, Ashour A, Yildirim G, Aldemir A, Sahmaran M. Properties of geopolymers sourced from construction and demolition waste: a review. J Build Eng. 2022;50(7):104104. doi:10.1016/j.jobe.2022.104104.
[14] Kan L, Wang F. Mechanical properties of high ductile alkali-activated fiber reinforced composites incorporating red mud under different curing conditions. Ceram Int. 2022;48(2):1999–2011. doi:10.1016/j.ceramint.2021.09.285.
[15] Provis JL, Palomo A, Shi C. Advances in understanding alkali-activated materials. Cem Concr Res. 2015;78:110–25. doi:10.1016/j.cemconres.2015.04.013.
[16] Wang F, Ma J, Ding Y, Yu J, Yu K. Engineered geopolymer composite (EGC) with ultra-low fiber content of 0.2%. Constr Build Mater. 2024;411(3):134626. doi:10.1016/j.conbuildmat.2023.134626.
[17] Duxson P, Fernández-Jiménez A, Provis JL, Lukey GC, Palomo A, van Deventer JS. Geopolymer technology: the current state of the art. J Mater Sci. 2006;42(9):2917–33. doi:10.1007/s10853-006-0637-z.
[18] Juenger MCG, Winnefeld F, Provis JL, Ideker JH. Advances in alternative cementitious binders. Cem Concr Res. 2011;41(12):1232–43. doi:10.1016/j.cemconres.2010.11.012.
[19] Lao JC, Huang BT, Fang Y, Xu LY, Dai JG, Shah SP. Strain-hardening alkali-activated fly ash/slag composites with ultra-high compressive strength and ultra-high tensile ductility. Cem Concr Res. 2023;165(1):107075. doi:10.1016/j.cemconres.2022.107075.
[20] Lao JC, Huang BT, Xu LY, Khan M, Fang Y, Dai JG. Seawater sea-sand engineered geopolymer composites (EGC) with high strength and high ductility. Cem Concr Compos. 2023;138(6):104998. doi:10.1016/j.cemconcomp.2023.104998.
[21] Liu J, Hao Y, Ren Q, Ma X, Yang R. Freeze-thaw performance of low-cost rubber crumb aggregate EGC: the influence of rubber particle size and KH550. Constr Build Mater. 2026;515(3):145651. doi:10.1016/j.conbuildmat.2026.145651.
[22] Zhang S, Yan Z, Xu G, Liu X, Zhu H, Jiang X. A comparative study on spalling behaviors of alkali-activated ultra-high performance concrete (AAUHPC) and cement-based UHPC. J Clean Prod. 2026;554:148084. doi:10.1016/j.jclepro.2026.148084.
[23] Jiang X, Xiao R, Bai Y, Huang B, Ma Y. Influence of waste glass powder as a supplementary cementitious material (SCM) on physical and mechanical properties of cement paste under high temperatures. J Clean Prod. 2022;340:130778. doi:10.1016/j.jclepro.2022.130778.
[24] Yuan Z, Yao Y, Lu C. Mechanical performance and mechanisms of recycled fine aggregate engineered geopolymer composites modified by *in-situ* generated nano-SiO_2. Constr Build Mater. 2026;533(2):146686. doi:10.1016/j.conbuildmat.2026.146686.
[25] Woo SY, Kim SJ, Kim S, Banthia N, Yoo DY. Sustainability and mechanical performance of hydrated lime-activated, strain-hardening slag composites incorporating crumb rubber. Cem Concr Compos. 2026;170(1):106576. doi:10.1016/j.cemconcomp.2026.106576.

[26] Zhang ZL, Yang ZM, Xu LY, Lao JC, Zhang H, Huang YJ, et al. Beyond performance-cost trade-off: engineered geopolymer composites (EGC) incorporating ultra-high-volume coal gangue wastes. J Clean Prod. 2026;570(1):148729. doi:10.1016/j.jclepro.2026.148729.
[27] Yan J, Zhong S, Chen S, Lv Y, Yang L, Peng G, et al. Study on the application of sediment-based embankment building and ultra-high-performance concrete (UHPC) preparation in the resource utilization of Yellow River sediment. Materials. 2022;15(16):5668. doi:10.3390/ma15165668.
[28] Jiang S, Xu J, Song Y, Gong W, Wang L, Yu Z, et al. Effect of calcination pretreatment on mechanical properties of alkali-activated artificial stone incorporating Yellow River silt. J Clean Prod. 2022;364(3):132682. doi:10.1016/j.jclepro.2022.132682.
[29] Wang H, Xu J, Song Y, Hou M, Xu Y. Development of low-cost engineered cementitious composites using Yellow River silt and unoiled PVA fiber. Constr Build Mater. 2024;425(4):136063. doi:10.1016/j.conbuildmat.2024.136063.
[30] Lu C, Pang Z, Chu H, Leung CKY. Experimental and numerical investigation on the long-term performance of engineered cementitious composites (ECC) with high-volume fly ash and domestic polyvinyl alcohol (PVA) fibers. J Build Eng. 2023;70:106324. doi:10.1016/j.jobe.2023.106324.
[31] Qiu X, Tang L, Shi Y, Li H, Wang T. Hybrid local fibers for enhancing the mechanical properties of engineered cementitious composites. Materials. 2026;19(13):2908. doi:10.3390/ma19132908.
[32] Zhou J, Qian S, Ye G, Copuroglu O, van Breugel K, Li VC. Improved fiber distribution and mechanical properties of engineered cementitious composites by adjusting the mixing sequence. Cem Concr Compos. 2012;34(3):342–8. doi:10.1016/j.cemconcomp.2011.11.019.
[33] GB/T17671-2021. Method of Testing Cements-Determination of strength. Beijing, China: Standards Association China; 2021. (In Chinese).
[34] Yi J, Wang L, Ma L, Zhang Q, Zhang J, Chi J. Experimental study on basic mechanical properties of PVA fiber-reinforced coral cement-based composites. Materials. 2023;16(7):2914. doi:10.3390/ma16072914.
[35] Ren B, Chai L, Liu Y, Wang Y. Preparation of high-ductility cement-calcined coal-gangue-powder-composite-based rapid repair material. Materials. 2023;16(17):6049. doi:10.3390/ma16176049.
[36] Murcia DH, Çomak B, Soliman E, Reda Taha MM. Flexural behavior of a novel textile-reinforced polymer concrete. Polymers. 2022;14(1):176. doi:10.3390/polym14010176.
[37] Wang C, Zhao X, Zhao J, Zhang X, Ying X, Li X. Effect of bottom ash powder replacement rate, water cement ratio and sand cement ratio on alkali activated slag mortar. Sci Rep. 2025;15(1):4061. doi:10.1038/s41598-025-87552-0.
[38] Li J, Dang X, Zhang J, Yi P, Li Y. Mechanical properties of fly ash-slag based geopolymer for repair of road subgrade diseases. Polymers. 2023;15(2):309. doi:10.3390/polym15020309.
[39] Lv Y, Wang C, Han W, Li X, Peng H. Study of the mechanical properties and microstructure of alkali-activated fly ash-slag composite cementitious materials. Polymers. 2023;15(8):1903. doi:10.3390/polym15081903.
[40] Dai S, Wang H, An S, Yuan L. Mechanical properties and microstructural characterization of metakaolin geopolymers based on orthogonal tests. Materials. 2022;15(8):2957. doi:10.3390/ma15082957.
[41] Alyousef R, Ebid AAK, Huseien GF, Mohammadhosseini H, Alabduljabbar H, Poi Ngian S, et al. Effects of sulfate and sulfuric acid on efficiency of geopolymers as concrete repair materials. Gels. 2022;8(1):53. doi:10.3390/gels8010053.
[42] Zhao X, Wang H, Jiang L, Meng L, Zhou B, Zhang J. Long-term physical and mechanical properties and microstructures of fly-ash-based geopolymer composite incorporating carbide slag. Materials. 2021;14(21):6692. doi:10.3390/ma14216692.
[43] Goracci G, Ogundiran MB, Barzegar M, Iturrospe A, Arbe A, Dolado JS. Kaolin clay-based geopolymer for ionic thermoelectric energy harvesting. ACS Omega. 2024;9(12):13728–37. doi:10.1021/acsomega.3c08257.